PCIM Europe 2023; International Exhibition and Conference for Power Electronics, Intelligent Motion, Renewable Energy and Energy Management; Proceedings of

DC Transformer Impact on Voltage Dynamics in Hybrid AC-DC Power Distribution Networks

J. Mace, R. Barcelos, M. Dupont, *et al.*

POWER ELECTRONICS LABORATORY
ÉCOLE POLYTECHNIQUE FÉDÉRALE DE LAUSANNE

 DOI:10.30420/566091272

pcim EUROPE

DC Transformer Impact on Voltage Dynamics in Hybrid AC-DC Power Distribution Networks

Jules Mace, Renan Pillon Barcelos, Max Dupont, Andrea Cervone, Drazen Dujic

École Polytechnique Fédérale de Lausanne (EPFL), Power Electronics Laboratory, Switzerland

Corresponding author: Jules Mace, jules.mace@epfl.ch

Abstract

AC/DC power distribution networks use various types of power converters to interconnect their buses, active front ends between AC and DC buses, and DC transformers between DC buses. Different active front end control methods, like voltage or power regulation, can be implemented to set the power flow throughout the DC network. They offer equivalent steady state but behave differently during transients. In this paper, power distribution networks with multiple active front end converters operating in various combinations of voltage and power-regulating modes are analyzed. This study shows that using only voltage-regulating active front ends results in slower transients when DC transformers are integrated in the power distribution network while power-regulating active front ends have faster transients but can cause much larger voltage overshoots. A parametric model that accurately estimates the network transient is developed and experimentally verified.

1 Introduction

Growth in the share of renewable energy resources in the energy mix is pushing for paradigm changes in the power distribution systems, among which is the change from AC-only power distribution networks (PDNs) to hybrid AC/DC PDNs [1]–[3] as illustrated in Fig. 1. AC and DC power sources (thermal power plants or solar and wind), storage (pumped hydro or battery-based...) and loads are employed, creating interconnected AC and DC subnetworks. This AC-DC interconnection is performed by active front ends (AFEs) [3]–[5] when bidirectional power flow is desired. Between AC buses, interconnection is typically achieved by conventional passive AC transformers while for DC buses, various converter-based solutions are proposed and one specific realization, namely the DC Transformer (DCT) is considered in this work.

The DC transformer is an isolated DC/DC converter designed to behave as the DC equivalent of the AC transformer by offering galvanic isolation and voltage adaptation. Since it is a power electronics-based converter, an active control is also often proposed to regulate its buses power flow and voltage level [6]–[9]. Other solutions, based on resonant topologies [10], [11], provide voltage adaptation and natural power flow without active regulation. The power flow and DC voltage regulation action are left to the surrounding converters at the buses, mainly the AFEs [10], [11].

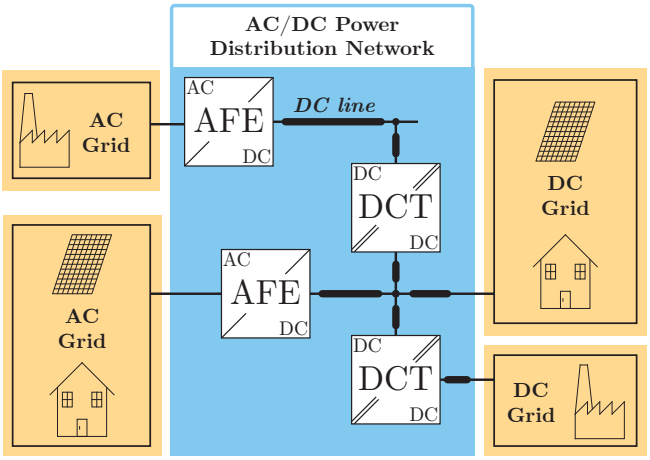

Fig. 1: Example of an hybrid AC/DC power distribution network with DC transformers interconnecting DC buses.

Those converters can control the bus power or the bus voltage [12]. When the AFE is set in

ISBN 978-3-8007-6091-6

power regulation (PR-AFE), it controls the power in its connected buses and to ensure voltage stability, another device must control the voltage. Instead, when the AFE is set in voltage regulation (VR-AFE), it controls the DC bus voltage, while external sources and loads create some power demand in the bus.

By connecting VR-AFEs, PR-AFEs and DCTs, it is possible to regulate the power flows and voltages across the network in many different ways. Resonant DCTs have been subject to substantial research resulting in their potential use in large scale networks and an assessment is necessary to evaluate their operational performances especially during power and voltage transients. Efficient designs [11] and parametric models [13] have been developed but not evaluated in real-world applications. Furthermore, the same power and voltage steady state can be achieved with multiple combinations of VR-AFEs and PR-AFEs but, because the control actions are different, the performance during transients is different as well.

This paper develops parametric models that are validated through experiments in a laboratory DC microgrid to compare and predict the impact of those two configurations on voltage and power dynamics when DCTs are employed. It is shown that the operating performances are largely dependent on the DC transformer equivalent circuit parameters, proportional to the losses, and the employed DC-link capacitances.

2 Considered Converters

The topology and the control structure of the converters used in this study are presented hereafter along with the relevant models and transfer functions for their application in DC grids.

2.1 Active Front End

The AFE considered in this study, shown in Fig. 2 can be set to either regulate the AC power or the DC voltage. When the AFE regulates the DC bus power (PR-AFE), a conventional single stage controller for AC currents regulation is implemented as in Fig. 2b, with a phase-locked loop (PLL) ensuring grid angle tracking. Meanwhile, when the

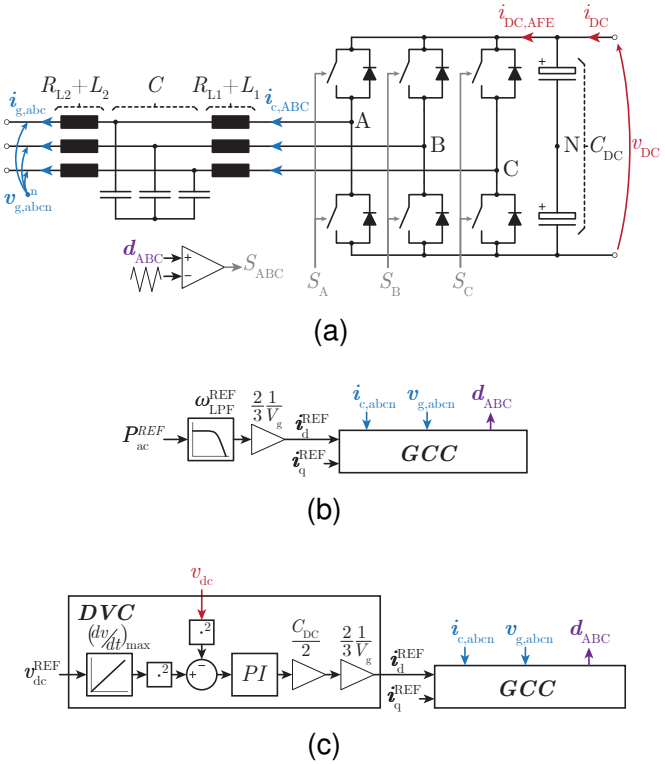

Fig. 2: Schemes of AFEs: (a) power stage, (b) controller of a PR-AFE and (c) controller of a VR-AFE.

AFE regulates the DC bus voltage (VR-AFE), a second stage DC voltage controller is added to regulate the voltage by adjusting the AC power reference, implemented as in Fig. 2c with a PI controller.

The VR-AFE controller transfer function is, when the grid current control dynamics are neglected:

$$T_{\mathrm{dvc}} = \frac{i_{\mathrm{dc,AFE}}}{v_{\mathrm{dc}}^{\mathrm{REF}} - v_{\mathrm{dc}}} = C_{\mathrm{DC}} \cdot \frac{K_{\mathrm{P,DVC}} s + K_{\mathrm{I,DVC}}}{s} \quad (1)$$

And the PR-AFE current transfer function is modeled as a low-pass filter:

$$G_{\mathrm{REF}} = \frac{i_{\mathrm{dc,AFE}}}{i_{\mathrm{dc,AFE}}^{\mathrm{REF}}} = \frac{P_{\mathrm{ac}}}{P_{\mathrm{ac}}^{\mathrm{REF}}} = \frac{\omega_{\mathrm{gcc}}}{s + \omega_{\mathrm{gcc}}} \quad (2)$$

with ω_{gcc} representing the current control bandwidth.

2.2 DC Transformer

The DCT considered in this paper is a bidirectional resonant converter based on the LLC topology as sketched in Fig. 3, operating near the resonant frequency. It is operated in open-loop by modulating only the primary-side or the secondary-side

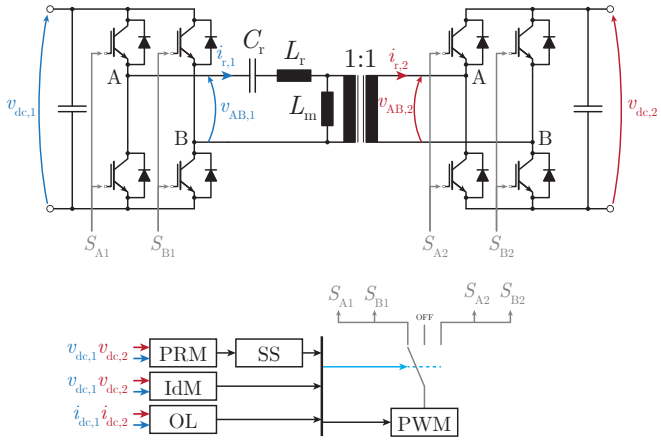

Fig. 3: DCT scheme with the power stage (LLC topology) and the controller stage, that includes a power reversal method (PRM), a soft-start (SS) function, an idle mode (IdM) detection function and an overcurrent limiter (OL).

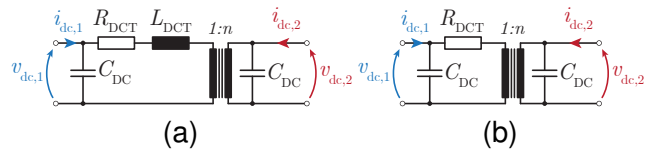

Fig. 4: (a) Model of the DCT [13] (b) Simplified model.

full-bridge, without any active closed-loop power flow regulation.

A DCT model is derived based on previous works [13] with the transformer equivalent capacitances, inductance and resistance to describe its behavior during transients. The DCT DC-link capacitances are ensuring low voltage ripples during switching. The resistance is associated to the losses in operation and is designed to be small. The inductance is approximately the resonant inductance L_r, part of the resonant tank that is having ringing at a frequency close to the switching frequency. As the time constant $\tau = \frac{L_r}{R_{\mathrm{DCT}}}$ is very small (around 4 µs in the DCTs of this study), the inductance can be neglected and hence, the model can be simplified to one shown in Fig. 4b.

3 DC System Modeling

A model is proposed in this section to estimate and predict the dynamic response of the system drawn in Fig. 1 for PDN configurations with mixed VR- and PR-AFEs using simple parameters: hardware values, AFE controller gains and DCT

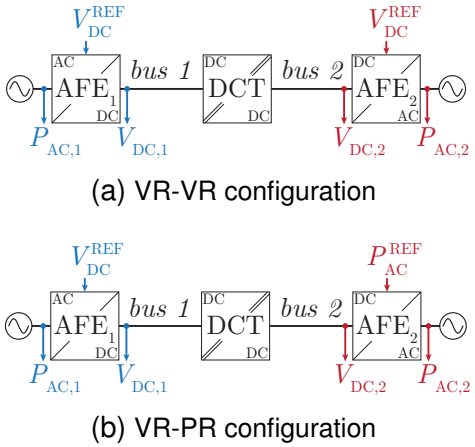

Fig. 5: Schemes of the simplified PDN configurations: (a) VR-VR configuration (b) VR-PR configuration.

characteristic performance (efficiency). To simplify the initial modeling, a reduced system comprised of two AFEs and one DCT is considered and in such system, as sketched in Fig. 5, two AFEs configurations are possible. In the first case, the two AFEs are set as VR-AFEs (VR-VR configuration) and the power flow is then regulated by adjusting the DC buses voltage difference. In a second case, one AFE is set as PR-AFE while the other is set as VR-AFE (VR-PR configuration).

3.1 Model for VR-VR Configuration

This model, illustrated in Fig. 6 combines the model of the AFE of (1) and the DCT model of Fig. 4. The DCT adds extra capacitance with:

$$C'_{\mathrm{DC}} = C_{\mathrm{DC,AFE}} + C_{\mathrm{DC,DCT}} \tag{3}$$

and the DCT resistance is responsible for a feedback loop along with an interaction between the two bus voltages $v_{\mathrm{dc},1}$ and $v_{\mathrm{dc},2}$. Based on Figs. 4b and 6a, the plant equations can be written as:

$$\underbrace{\begin{bmatrix} v_{\mathrm{dc},1} \\ v_{\mathrm{dc},2} \end{bmatrix}}_{\boldsymbol{v}_{\mathrm{dc}}} = \underbrace{\left(\boldsymbol{C}'s + \boldsymbol{R}_{\mathrm{DCT}}^{-1}\right)^{-1}}_{\boldsymbol{H}} \cdot \underbrace{\begin{bmatrix} i_{\mathrm{AFE},1} \\ i_{\mathrm{AFE},2} \end{bmatrix}}_{\boldsymbol{i}_{\mathrm{AFE}}} \tag{4}$$

with:

$$\begin{cases} \boldsymbol{C}' = C'_{\mathrm{DC}} \cdot \begin{bmatrix} 1 & 0 \\ 0 & 1 \end{bmatrix} \\ \boldsymbol{R}_{\mathrm{DCT}}^{-1} = \frac{1}{R_{\mathrm{DCT}}} \cdot \begin{bmatrix} 1 & -1 \\ -1 & 1 \end{bmatrix} \end{cases} \tag{5}$$

One thing that can be noticed is that the DCT connecting two DC lines introduces a pole in the plant transfer function, whose value is dependent on the capacitances and DCT resistance.

The AFE controller transfer function $\boldsymbol{T}'_{\mathrm{dvc}}$, on the other hand, can be written as:

$$\boldsymbol{i}_{\mathrm{AFE}} = \underbrace{\frac{K_{\mathrm{P,DVC}}\, s + K_{\mathrm{I,DVC}}}{s} C_{\mathrm{DC,AFE}} \begin{bmatrix} 1 & 0 \\ 0 & 1 \end{bmatrix}}_{\boldsymbol{T}'_{\mathrm{dvc}}} \underbrace{\begin{bmatrix} v_{\mathrm{dc},1}^{\mathrm{REF}} - v_{\mathrm{dc},1} \\ v_{\mathrm{dc},2}^{\mathrm{REF}} - v_{\mathrm{dc},2} \end{bmatrix}}_{\boldsymbol{v}_{\mathrm{dc}}^{\mathrm{REF}} - \boldsymbol{v}_{\mathrm{dc}}} \tag{6}$$

Combining (4) and (6), the reference-to-actual DC voltage transfer function $\boldsymbol{G}_{\mathrm{dvc}}$ is:

$$\begin{aligned} \boldsymbol{v}_{\mathrm{dc}} &= \boldsymbol{H} \cdot \boldsymbol{T}'_{\mathrm{dvc}} \cdot \left(\boldsymbol{v}_{\mathrm{dc}}^{\mathrm{REF}} - \boldsymbol{v}_{\mathrm{dc}}\right) \\ &= \underbrace{\left[\boldsymbol{I}_2 + \boldsymbol{H} \cdot \boldsymbol{T}'_{\mathrm{dvc}}\right]^{-1} \cdot \boldsymbol{H} \cdot \boldsymbol{T}'_{\mathrm{dvc}}}_{\boldsymbol{G}_{\mathrm{dvc}}} \cdot \boldsymbol{v}_{\mathrm{dc}}^{\mathrm{REF}} \end{aligned} \tag{7}$$

And the voltage-to-power transfer function $\boldsymbol{G}_{\mathrm{Vdc,P}}$ is:

$$\boldsymbol{P}_{\mathrm{ac}} = \underbrace{V_{\mathrm{dc}} \cdot \boldsymbol{T}'_{\mathrm{dvc}} \cdot \left(\boldsymbol{I}_2 - \boldsymbol{G}_{\mathrm{dvc}}\right)}_{\boldsymbol{G}_{\mathrm{Vdc,P}}} \cdot \boldsymbol{v}_{\mathrm{dc}}^{\mathrm{REF}} \tag{8}$$

In Fig. 7, the impact of the DCT capacitance and resistance on the transfer functions is analyzed. When the DCT resistance increases, the magnitude of the cross-coupling term G_{dvc}^{21} decreases. In the same time, the magnitude of the direct term G_{dvc}^{22} is increasing, which results in better voltage reference tracking up to higher frequencies. So, large DCT resistance, despite also meaning an inefficient DCT, reduces the cross-coupling and improves the direct reference dynamics. Looking at the low-frequency part of the voltage to power transfer function $\boldsymbol{G}_{\mathrm{Vdc,P}}$, the magnitude of both the direct and cross-coupling terms is dropping with the increase of DCT resistance. Note that, in practice, the losses change with the operating point and hence this DCT resistance can greatly vary and the model must be adapted. As for the capacitance, it plays mainly a role at frequencies above 3 Hz.

3.2 Model for VR-PR Configuration

The plant can be modeled the same way as for the VR-VR configuration so (4) is still valid but since

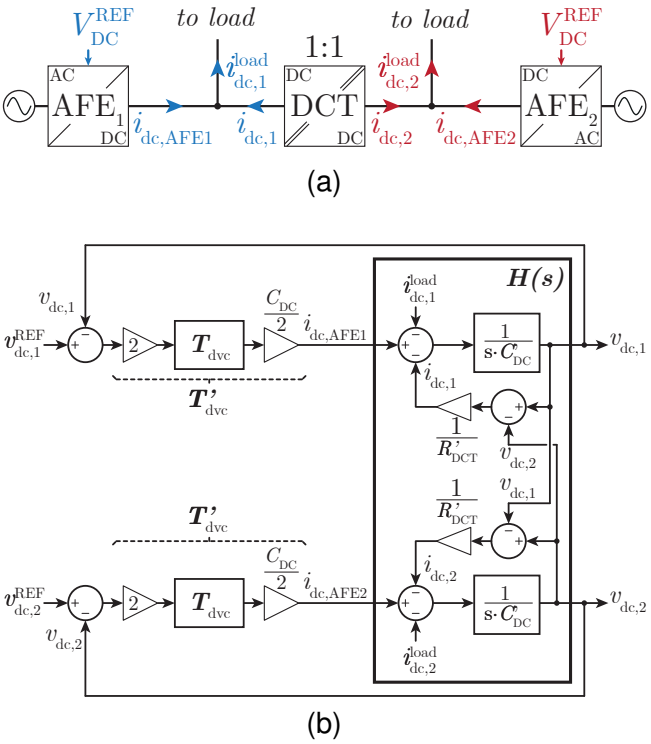

Fig. 6: Simplified DC System in VR-VR configuration: (a) system layout (b) derived control loop.

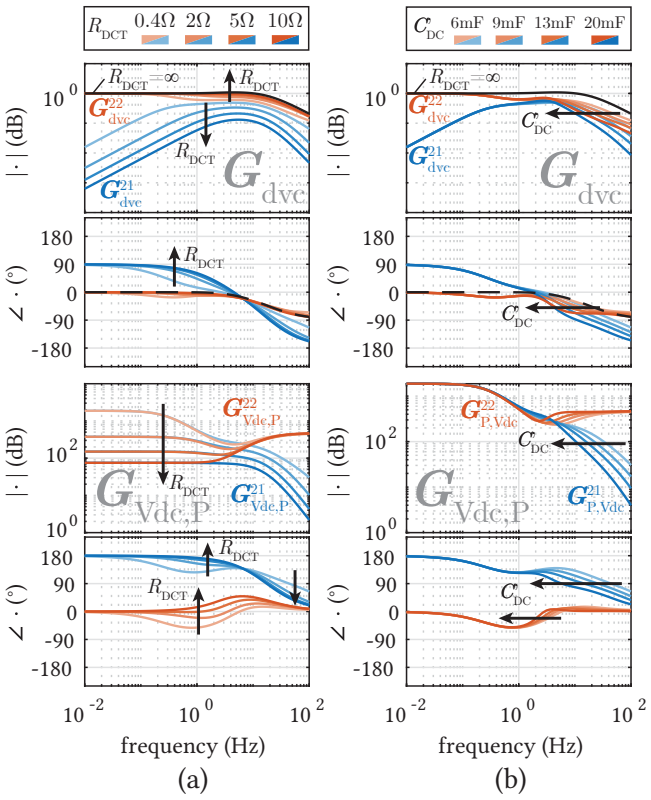

Fig. 7: Bode plots for the PDN transfer functions in VR-VR configuration for: (a) different R_{DCT} values and (b) different C'_{DC} values.

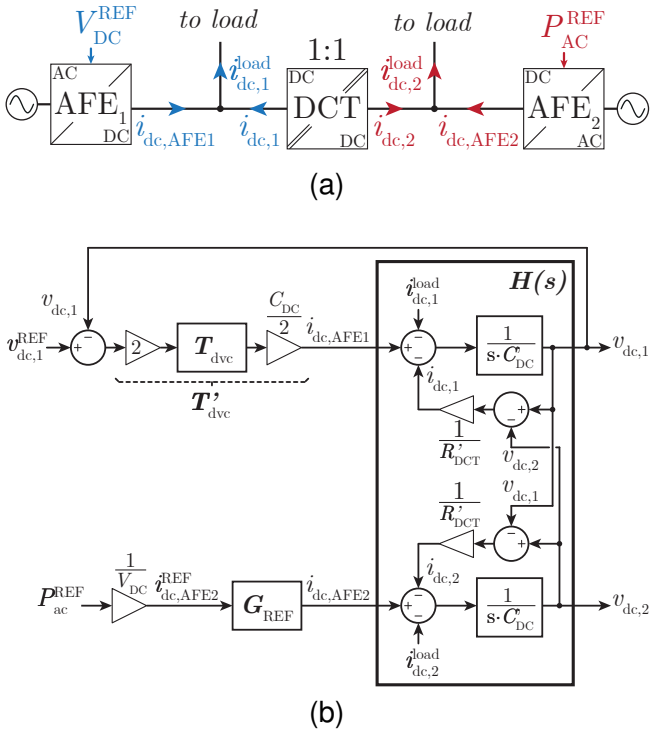

Fig. 8: Simplified DC System in VR-PR configuration: (a) system layout, (b) derived control loop.

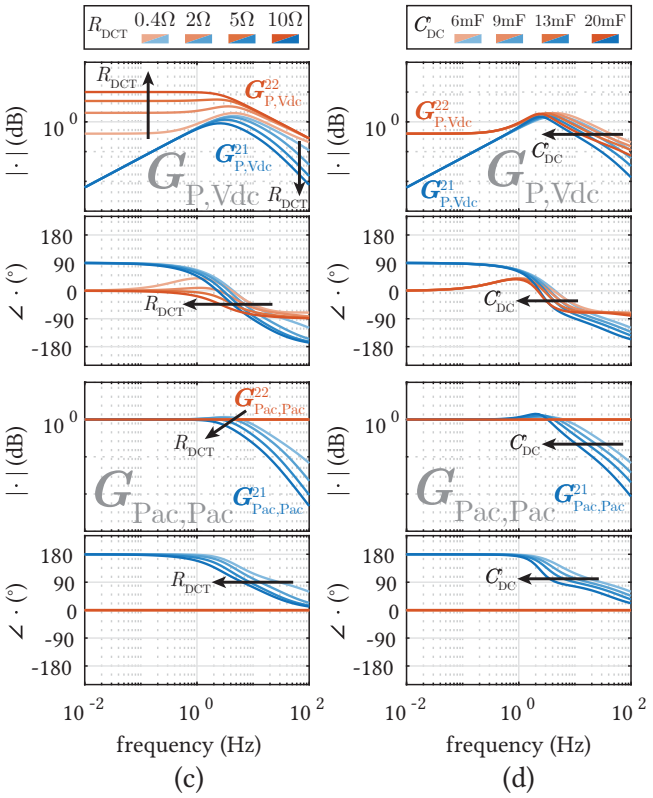

Fig. 9: Bode plots for the PDN transfer functions in VR-PR configuration for: (a) different R_{DCT} values and (b) different C'_{DC} values.

AFE$_1$ is in VR mode while AFE$_2$ is in PR mode, the control loop, sketched as in Fig. 8b, must be splitted between the AFE$_1$ voltage control action and the AFE$_2$ current control action. The DC voltage is thus:

$$\boldsymbol{v}_{\mathrm{dc}} = \boldsymbol{H} \cdot \Bigg(\underbrace{G_{\mathrm{REF}} \begin{bmatrix} 0 & 0 \\ 0 & 1 \end{bmatrix}}_{\boldsymbol{G}_{\mathrm{I}}} \boldsymbol{i}_{\mathrm{AFE}}^{\mathrm{REF}} + \underbrace{T'_{\mathrm{dvc}} \cdot \begin{bmatrix} 1 & 0 \\ 0 & 0 \end{bmatrix}}_{\boldsymbol{G}_{\mathrm{V}}} \cdot (\boldsymbol{v}_{\mathrm{dc}}^{\mathrm{REF}} - \boldsymbol{v}_{\mathrm{dc}}) \Bigg) \tag{9}$$

Based on that, the power reference-to-voltage transfer function $\boldsymbol{G}_{\mathrm{P,Vdc}}$ is:

$$\begin{aligned} \boldsymbol{v}_{\mathrm{dc}} &= (\boldsymbol{I}_2 + \boldsymbol{H} \cdot \boldsymbol{G}_{\mathrm{V}})^{-1} \cdot \boldsymbol{G}_{\mathrm{I}} \cdot \boldsymbol{i}_{\mathrm{AFE}}^{\mathrm{REF}} \\ &= \underbrace{(\boldsymbol{I}_2 + \boldsymbol{H} \cdot \boldsymbol{G}_{\mathrm{V}})^{-1} \cdot \boldsymbol{G}_{\mathrm{I}} \cdot \frac{1}{V_{\mathrm{dc}}}}_{\boldsymbol{G}_{\mathrm{P,Vdc}}} \cdot \boldsymbol{P}_{\mathrm{ac}}^{\mathrm{REF}} \end{aligned} \tag{10}$$

And the power transfer function $\boldsymbol{G}_{\mathrm{Pac,Pac}}$ is:

$$\boldsymbol{P}_{\mathrm{ac}} = \underbrace{(\boldsymbol{I}_2 + \boldsymbol{G}_{\mathrm{V}} \cdot \boldsymbol{H})^{-1} \cdot \boldsymbol{G}_{\mathrm{I}}}_{\boldsymbol{G}_{\mathrm{Pac,Pac}}} \cdot \boldsymbol{P}_{\mathrm{ac}}^{\mathrm{REF}} \tag{11}$$

$G_{\mathrm{Pac,Pac}}$ and $G_{\mathrm{P,Vdc}}$ are modeling the system response to a power reference step in AFE$_2$. In Fig. 9, Bode plots of the transfer functions are drawn for different DCT capacitance and resistance values. As it can be seen, the low frequency magnitude of the $G^{22}_{\mathrm{P,Vdc}}$ increases with the resistance. At higher frequencies, the DCT resistance is however having minor impacts on the direct term, but as it increases, the cross-coupling decreases. Hence, large DCT resistance is expected to have little impact on the direct term voltage dynamics but it could improve the cross-coupling transients. The $G_{\mathrm{Pac,Pac}}$ cut-off frequency is also decreasing as the resistance increases. The capacitance has mainly an effect on the cut-off frequency for both $G_{\mathrm{P,Vdc}}$ and $G_{\mathrm{Pac,Pac}}$: as the capacitance increases, the cut-off frequency is decreased.

4 Extension to Larger PDNs

Considering larger PDNs with more than two AFEs and more than one DCT, the transfer functions presented in (9) to (11) are still valid but the matrices $\boldsymbol{H}$, $\boldsymbol{G}_{\mathrm{V}}$ and $\boldsymbol{G}_{\mathrm{I}}$ must be adapted.

Firstly, the plant transfer function $\boldsymbol{H}$ presented in (4) becomes:

$$\underbrace{\begin{bmatrix} v_{\mathrm{dc},1} \\ \dots \\ v_{\mathrm{dc,n}} \end{bmatrix}}_{\boldsymbol{v}_{\mathrm{dc}}} = \underbrace{\left(\boldsymbol{C}'s + \boldsymbol{R}_{\mathrm{DCT}}^{-1}\right)^{-1}}_{\boldsymbol{H}} \cdot \underbrace{\begin{bmatrix} i_{\mathrm{AFE},1} \\ \dots \\ i_{\mathrm{AFE,n}} \end{bmatrix}}_{\boldsymbol{i}_{\mathrm{AFE}}} \tag{12}$$

where n is the number of buses in the system. $\boldsymbol{C}$ is the capacitance matrix:

$$\boldsymbol{C}' = \begin{bmatrix} \ddots & & 0 \\ & C'_{\mathrm{DC},i} & \\ 0 & & \ddots \end{bmatrix} \tag{13}$$

where $C_{\mathrm{DC},i}$ is the sum of all the capacitances connected to bus i, this may include AFEs and DCTs DC-link capacitances. $\boldsymbol{R}_{\mathrm{DCT}}^{-1}$ is the admittance matrix:

$$\boldsymbol{R}_{\mathrm{DCT}}^{-1} = \begin{bmatrix} \ddots & & -\frac{1}{R_{\mathrm{DCT},ij}} \\ & \sum_k \frac{1}{R_{\mathrm{DCT},ik}} & \\ -\frac{1}{R_{\mathrm{DCT},ij}} & & \ddots \end{bmatrix} \tag{14}$$

where $R_{\mathrm{DCT},ij}$ is the resistance of the DCT connected between bus i and j.

Secondly, considering a system with n_{VR} VR-AFEs and n_{PR} PR-AFEs, (9) can be re-written as:

$$\boldsymbol{v}_{\mathrm{dc}} = \boldsymbol{H} \cdot \left(\boldsymbol{G}_{\mathrm{I}} \cdot \boldsymbol{i}_{\mathrm{AFE}}^{\mathrm{REF}} + \boldsymbol{G}_{\mathrm{V}} \cdot \left(\boldsymbol{v}_{\mathrm{dc}}^{\mathrm{REF}} - \boldsymbol{v}_{\mathrm{dc}}\right)\right) \tag{15}$$

with:

$$\boldsymbol{G}_{\mathrm{V}} = \begin{bmatrix} \ddots & & 0 \\ & T'_{\mathrm{dvc},i} & \\ 0 & & \ddots \end{bmatrix}, \boldsymbol{G}_{\mathrm{I}} = \begin{bmatrix} \ddots & & 0 \\ & G_{\mathrm{REF},i} & \\ 0 & & \ddots \end{bmatrix} \tag{16}$$

where $T'_{\mathrm{dvc},i}$ is the AFE$_i$ DC voltage controller transfer function and $G_{\mathrm{REF},i}$ is the AFE$_i$ power reference transfer function.

The voltage and power equations for VR-VR and VR-PR configurations (9,7,8, 10,11) can then be combined into a new set of generalized equations. The impact of references on the voltages can be written as:

$$\begin{aligned} \boldsymbol{v}_{\mathrm{dc}} = &\underbrace{\left(\boldsymbol{I}_{\mathrm{n}} + \boldsymbol{H} \cdot \boldsymbol{G}_{\mathrm{V}}\right)^{-1} \cdot \boldsymbol{H} \cdot \boldsymbol{G}_{\mathrm{V}}}_{\boldsymbol{G}_{\mathrm{dvc}}} \cdot \boldsymbol{v}_{\mathrm{dc}}^{\mathrm{REF}} \\ &+ \underbrace{\left(\boldsymbol{I}_{\mathrm{n}} + \boldsymbol{H} \cdot \boldsymbol{G}_{\mathrm{V}}\right)^{-1} \cdot \boldsymbol{H} \cdot \boldsymbol{G}_{\mathrm{I}} \cdot \boldsymbol{V}_{\mathrm{DC}}^{-1}}_{\boldsymbol{G}_{\mathrm{P,Vdc}}} \cdot \boldsymbol{P}_{\mathrm{ac}}^{\mathrm{REF}} \end{aligned} \tag{17}$$

And the impact of the references on the powers can be written as:

$$\begin{aligned} \boldsymbol{P}_{\mathrm{ac}} = &\underbrace{\boldsymbol{V}_{\mathrm{DC}} \cdot \boldsymbol{G}_{\mathrm{V}} \cdot \left(\boldsymbol{I}_2 - \boldsymbol{G}_{\mathrm{dvc}}\right)}_{\boldsymbol{G}_{\mathrm{dvc}}} \cdot \boldsymbol{v}_{\mathrm{dc}}^{\mathrm{REF}} \\ &+ \underbrace{\left(\boldsymbol{I}_{\mathrm{n}} + \boldsymbol{G}_{\mathrm{V}} \cdot \boldsymbol{H}\right)^{-1} \cdot \boldsymbol{G}_{\mathrm{I}}}_{\boldsymbol{G}_{\mathrm{Pac,Pac}}} \cdot \boldsymbol{P}_{\mathrm{ac}}^{\mathrm{REF}} \end{aligned} \tag{18}$$

So, by computing $\boldsymbol{H}$, $\boldsymbol{G}_{\mathrm{V}}$ and $\boldsymbol{G}_{\mathrm{I}}$ based on the element parameters, the transfer functions that characterize the system voltage and power dynamics can be obtained for all mixed VR- and PR-AFEs configurations.

5 Experimental Validation

A power distribution system composed of four DC buses enabled by four AFEs and three DCTs as sketched in Fig. 10 is considered. The four AFEs used are presented in Fig. 10b. Figs. 10c and 10d show one AFE unit and one DCT unit, respectively. AFE hardware parameter values are presented in Tab. 1. The chosen controller gain values for the DC voltage controller (DVC), the grid current controller (GCC) and the PLL are summarized in Tab. 2.

As for the DCT, to enable the use of DCT in grids, various features are additionally implemented. A power reversal method (PRM) achieves seamless power reversal when conditions to do so are detected in DC grid [11], [14]. To improve the DCT efficiency at low power, an idle mode (IdM) is activated when zero current operation is detected. An overcurrent limiter (OL) [15] is limiting the current in the resonant tank to avoid damages on the active stage. Finally, every time DCT is started and to avoid excessive inrush currents, a soft-start (SS) is implemented [11].

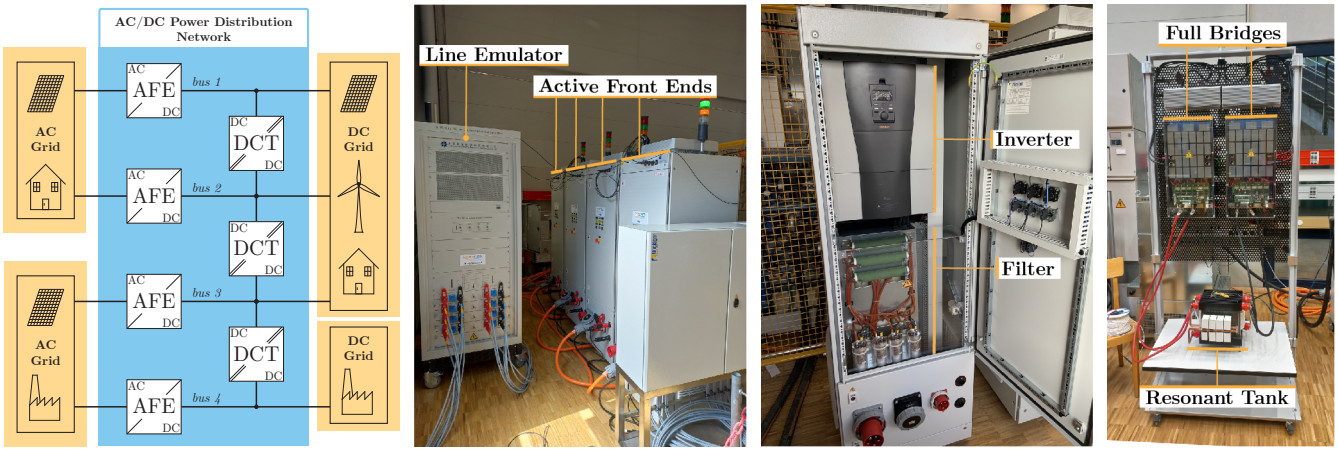

Fig. 10: Hybrid AC/DC distribution system considered (a) scheme, (b) four active front ends and line emulator (c) active front end elements, (d) DC transformer.

Tab. 1: AFE Parameters

Parameter	Value
f_{SW}	8 kHz
L_1	600 µH
R_{L1}	66 mΩ
C	100 µF
L_2	300 µH
R_{L2}	33 mΩ
$C_{\mathrm{DC,AFE}}$	4.7 mF

Tab. 2: AFE Controller Gains

Gain	Value
f_{Sampling}	8 kHz
ω_{GCC}	2.67 krad s^{-1}
$K_{\mathrm{P,DVC}}$	133
$K_{\mathrm{I,DVC}}$	2133
$(\frac{dv}{dt})_{\mathrm{max}}$	200 V s^{-1}
$K_{\mathrm{P,PLL}}$	92
$K_{\mathrm{I,PLL}}$	4232

Tab. 3: DCT Parameters

Parameter	Value
f_{SW}	10 kHz
C_{r}	37.5 µF
L_{r}	11.6 µH
L_{m}	750 µH
f_{r}	10.7 kHz
n	1
$C_{\mathrm{DC,DCT}}$	1.02 mF

5.1 VR-VR Model Validation

The responses modeled by $\boldsymbol{G}_{\mathrm{dvc}}$ and $\boldsymbol{G}_{\mathrm{Vdc,P}}$ are compared to the experimental results in Fig. 11. As it can be seen, the step response computed using the model transfer function is close to the experimental response. Both the shape and the response time are matching, the initial voltage drop is well modeled (AFE_1: experimentally voltage drop of 5 V compared to 7 V in the model, AFE_2: experimentally drop of 13 V compared to 10 V in the model) and the settling times are very close (approximately 1 s).

This model explains why transients in a VR-VR configuration are so long. The DCT resistance introduces a feedback in the plant model that significantly damps the response of an AFE DC voltage controller based on a PI regulator.

5.2 VR-PR Model Validation

The step response modeled by $G_{\mathrm{P,Vdc}}$ and $G_{\mathrm{Pac,Pac}}$ are compared to the experimental results in Fig. 12. It can be seen that the model matches very well with the experimental results with the same response time (settling time of around 100 ms for both modeled and experimental voltage response) and characteristic shape (similar value for the initial voltage drop (18 V for $v_{\mathrm{dc},1}$) for both the model and the experiments).

This model can therefore reliably predict the significant voltage drop caused by power steps in the bus, originated by AFEs or any DC load or source. An increase in the DC bus capacitance or the DCT resistance reduces the voltage drop but will also results in a slower voltage response.

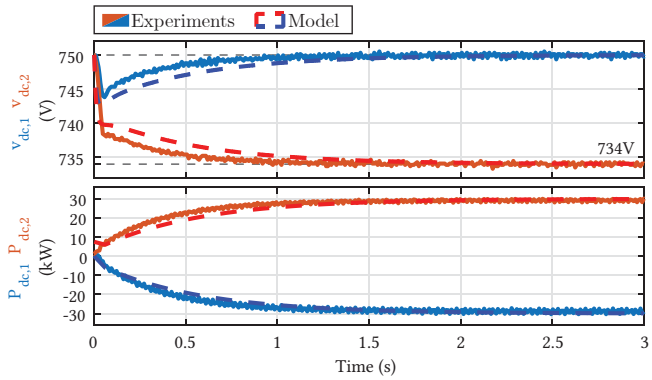

Fig. 11: Comparison of modeled and experimental power step responses for the VR-VR configuration for a voltage reference step in AFE_2 (750 V to 734 V).

Tab. 4: Power and Voltage Steps for Schemes Comparison

Test	$V_{\mathrm{dc},2}^{\mathrm{ini}} \rightarrow V_{\mathrm{dc},2}^{\mathrm{fin}}$	$P_{\mathrm{AC},2}^{\mathrm{ini}} \rightarrow P_{\mathrm{AC},2}^{\mathrm{fin}}$	$R_{12}^{\mathrm{eq}*}$
①	750 V → 742 V	0 kW → 10 kW	0.59 Ω
②	750 V → 737 V	0 kW → 20 kW	0.46 Ω
③	750 V → 734 V	0 kW → 30 kW	0.40 Ω

*R_{12}^{eq} is obtained by the formula $\frac{V_{\mathrm{dc},1} \cdot \left(V_{\mathrm{dc},1} - V_{\mathrm{dc},2}^{\mathrm{fin}}\right)}{P_{\mathrm{ac},2}^{\mathrm{fin}}}$

5.3 Comparison and Discussion

To compare the two configurations, power steps of up to 30 kW are performed. Voltage and power reference values are summarized in Tab. 4. The resulting waveforms are shown in Fig. 13. In the VR-VR configuration, the voltage and power settling time is much slower compared to the VR-PR configuration. It takes from 0.78 s to 1.10 s for the voltage to settle in the VR-VR configuration when it takes only 100 ms for the VR-PR configuration. However, in the VR-PR configuration, a very large initial voltage drop is occurring as the power settles in around 50 ms. This voltage drop is much larger in AFE_2, more than twice the one in AFE_1. The voltage settling time, around 100 ms is also significantly faster than in the VR-VR configuration.

Another thing that can be noticed is that the equivalent resistance R_{12}^{eq}, compiled in Tab. 4, between the two AFEs decreases with the power step. As predicted by the VR-VR model, this impacts significantly the response of the VR-VR configuration, with a settling time that increases as the power increases and the DCT resistance decreases. In the VR-PR configuration, the DCT resistance on the other hand affects very little the voltage and power response.

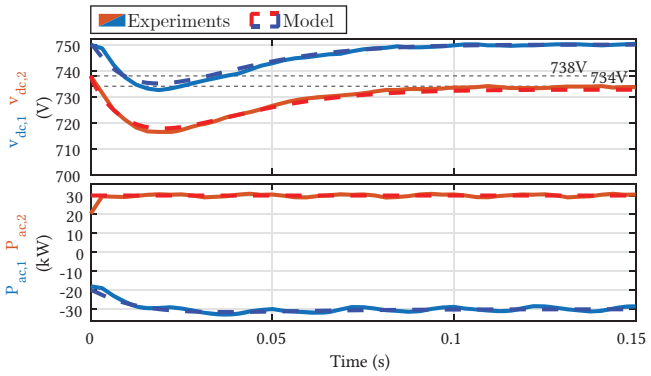

Fig. 12: Comparison of modeled and experimental power step responses for the VR-PR configuration for a power reference step in AFE_2 (20 kW to 30 kW, with a non-filtered step of power reference ($G_{\mathrm{REF}}(s) = 1$)).

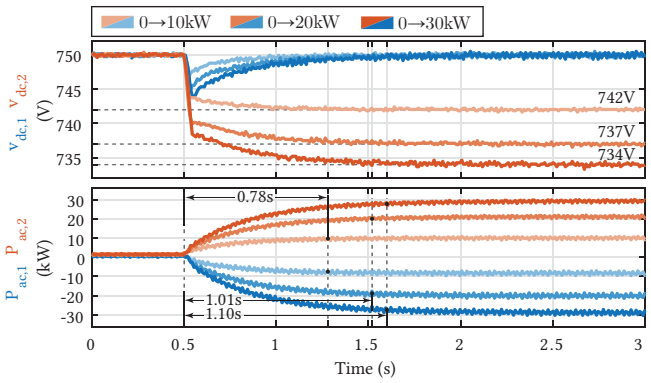

(a) VR-VR Configuration

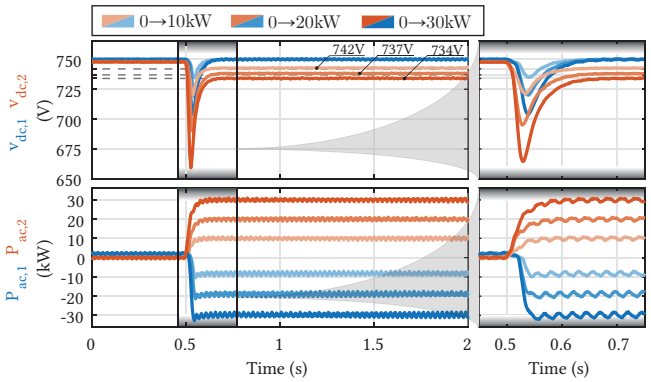

(b) VR-PR configuration

Fig. 13: Power steps of Tests ①, ② and ③: (a) VR-VR configuration: voltage steps of AFE_2 from 750 V to 742 V, 737 V, 734 V (b) VR-PR configuration: power steps of AFE_2 from 0 kW to 10 kW, 20 kW, 30 kW. $V_{\mathrm{dc},1}^{\mathrm{REF}}$ is kept at 750 V.

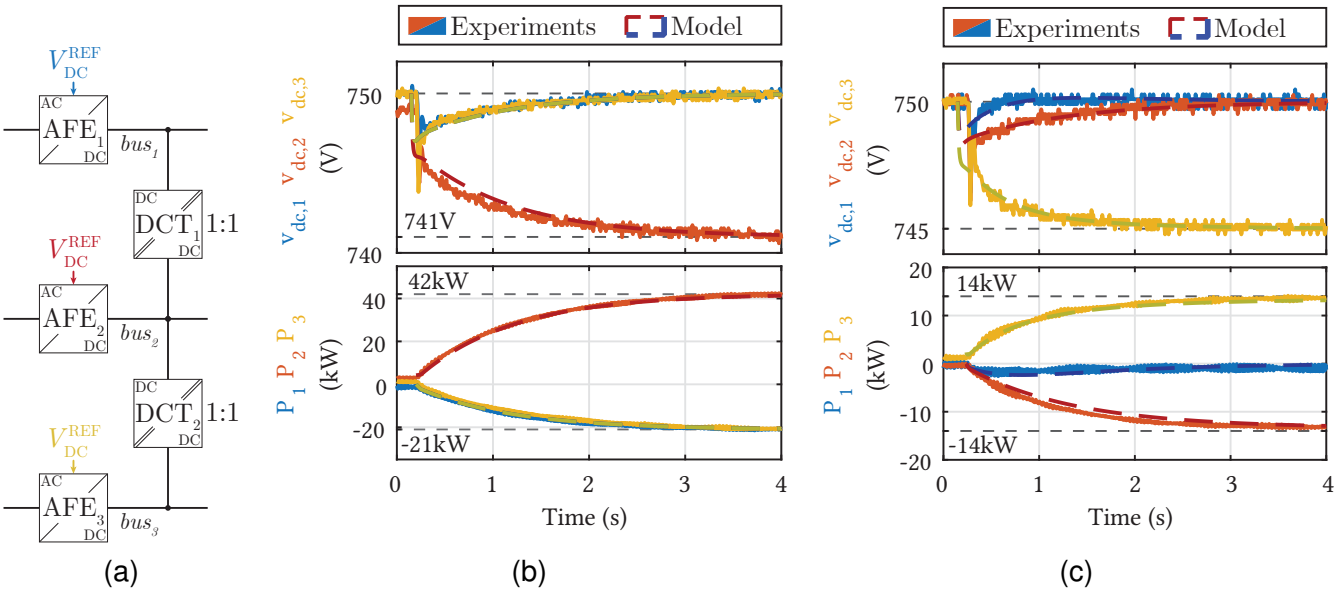

Fig. 14: Step response to voltage steps in a three bus system (a) scheme with three AFEs and two DCTs, step response to a voltage reference step for (b) AFE_2 (750 V to 741 V), (c) AFE_3 (750 V to 745 V).

The VR-PR configuration is thus faster (smaller settling time) than the VR-VR configuration but it suffers from larger voltage drops. The VR-VR configuration response is also significantly damped by the DCT resistance (the lower the DCT resistance, the larger the damping).

5.4 Extended System Model Validation

The model extension is validated with experiments for a larger system in VR-VR-VR configuration with two DCTs as shown in Fig. 14. The AFEs are identical to the AFE of Fig. 10c (same ratings, same hardware values, same controller gains) and the two DCTs have similar characteristics ($R_{\mathrm{DCT}}, C_{\mathrm{DC,DCT}}$) as the DCT of Fig. 10d. Response to a voltage reference step in bus 2 and bus 3 is compared with the model response. For both steps, the modeled response is matching the experimental response with a voltage settling time of around 3 s and a similar shape with the initial voltage drop followed by a slower settling time. This hence validates the extended system model.

6 Conclusion

In AC-DC PDNs, AFEs are controlling AC-to-DC bus power flows and DC bus voltages and therefore play a crucial role in the power flow stability and dynamics. When resonant DCTs are introduced as a new way to interconnect DC buses, they affect the system configuration and dynamics. As those DCTs are providing AC transformer-like natural power flow behavior, AFEs can be mixed in configurations involving more than one voltage-regulating AFE (VR-AFE).

The system dynamic response is, based on a parametric model and experiments, very slow when only VR-AFEs are controlling the grid power flows compared to when the PR-AFEs are employed. In the meantime, PR-AFE power reference steps induce very large initial voltage drops (or spikes). Hence, the decision between using PR-AFEs or VR-AFEs for power flow control is a choice between slow response time and initial voltage drops.

The DCT resistance, associated with the DCT efficiency, is having a large impact on the response of the VR-AFE response time. The larger it is, the faster the PDN voltage and the power reach the steady state for a VR-AFE voltage reference step. But larger DCT resistances imply larger losses therefore, a trade-off between DCT efficiency and fast PDN dynamics must be found when VR-AFEs are employed.

Acknowledgments

This project has been supported by the European project HYPERRIDE under Grant agreement ID: 957788.

References

[1] X. Liu, P. Wang, and P. C. Loh, "A Hybrid AC/DC Microgrid and Its Coordination Control," *IEEE Transactions on Smart Grid*, vol. 2, no. 2, pp. 278–286, Jun. 2011. DOI: 10.1109/TSG.2011.2116162.

[2] J. Hofer, B. Svetozarevic, and A. Schlueter, "Hybrid AC/DC building microgrid for solar PV and battery storage integration," in *2017 IEEE Second International Conference on DC Microgrids (ICDCM)*, Jun. 2017, pp. 188–191. DOI: 10.1109/ICDCM.2017.8001042.

[3] J. Yu, W. Ming, L. Haitao, L. Yang, and Z. Ying, "Bidirectional Droop Control of Interlinking Converter in AC/DC Hybrid Micro-Grid," in *2016 3rd International Conference on Information Science and Control Engineering (ICISCE)*, Jul. 2016, pp. 879–883. DOI: 10.1109/ICISCE.2016.192.

[4] X. Lu, J. Guerrero, R. Teodorescu, T. Kerekes, K. Sun, and L. Huang, "Control of parallel-connected bidirectional AC-DC converters in stationary frame for microgrid application," in *2011 IEEE Energy Conversion Congress and Exposition*, ISSN: 2329-3748, Sep. 2011, pp. 4153–4160. DOI: 10.1109/ECCE.2011.6064335.

[5] K. Zhou, Q. Jin, Z. Lan, C. Tu, M. Guo, and G. Liu, "The study of power electronic transformer on power flow control and voltage regulation in DC micro-grid," in *2015 5th International Conference on Electric Utility Deregulation and Restructuring and Power Technologies (DRPT)*, Nov. 2015, pp. 2166–2172. DOI: 10.1109/DRPT.2015.7432608.

[6] X. Li, L. Guo, Y. Li, C. Hong, Y. Zhang, *et al.*, "Flexible Interlinking and Coordinated Power Control of Multiple DC Microgrids Clusters," *IEEE Transactions on Sustainable Energy*, vol. 9, no. 2, pp. 904–915, Apr. 2018. DOI: 10.1109/TSTE.2017.2765681.

[7] S. Gao, H. Jia, and C. Marnay, "Techno-Economic Evaluation of Mixed AC and DC Power Distribution Network for Integrating Large-Scale Photovoltaic Power Generation," *IEEE Access*, vol. 7, pp. 105 019–105 029, 2019. DOI: 10.1109/ACCESS.2019.2931985.

[8] B. Liu, W. Wu, C. Zhou, C. Mao, D. Wang, *et al.*, "An AC–DC Hybrid Multi-Port Energy Router With Coordinated Control and Energy Management Strategies," *IEEE Access*, vol. 7, pp. 109 069–109 082, 2019. DOI: 10.1109/ACCESS.2019.2933469.

[9] Q. Ye, R. Mo, and H. Li, "Impedance Modeling and DC Bus Voltage Stability Assessment of a Solid-State-Transformer-Enabled Hybrid AC–DC Grid Considering Bidirectional Power Flow," *IEEE Transactions on Industrial Electronics*, vol. 67, no. 8, pp. 6531–6540, Aug. 2020. DOI: 10.1109/TIE.2019.2937039.

[10] J. Huang, J. Xiao, C. Wen, P. Wang, and A. Zhang, "Implementation of Bidirectional Resonant DC Transformer in Hybrid AC/DC Micro-Grid," *IEEE Transactions on Smart Grid*, vol. 10, no. 2, pp. 1532–1542, Mar. 2019. DOI: 10.1109/TSG.2017.2771822.

[11] J.-H. Jung, H.-S. Kim, M.-H. Ryu, and J.-W. Baek, "Design Methodology of Bidirectional CLLC Resonant Converter for High-Frequency Isolation of DC Distribution Systems," *IEEE Transactions on Power Electronics*, vol. 28, no. 4, pp. 1741–1755, Apr. 2013. DOI: 10.1109/TPEL.2012.2213346.

[12] J. Wang, C. Jin, and P. Wang, "A Uniform Control Strategy for the Interlinking Converter in Hierarchical Controlled Hybrid AC/DC Microgrids," *IEEE Transactions on Industrial Electronics*, vol. 65, no. 8, pp. 6188–6197, Aug. 2018. DOI: 10.1109/TIE.2017.2784349.

[13] J. E. Huber, J. Miniböck, and J. W. Kolar, "Generic Derivation of Dynamic Model for Half-Cycle DCM Series Resonant Converters," *IEEE Transactions on Power Electronics*, vol. 33, no. 1, pp. 4–7, Jan. 2018. DOI: 10.1109/TPEL.2017.2703300.

[14] R. P. Barcelos, J. Kucka, and D. Dujic, "Power Reversal Algorithm for Resonant Direct Current Transformers for DC Networks," *IEEE Access*, vol. 10, pp. 127 117–127 127, 2022, Conference Name: IEEE Access. DOI: 10.1109/ACCESS.2022.3225673.

[15] J. Kucka and D. Dujic, "Current Limiting in Overload Conditions of an LLC-Converter-Based DC Transformer," *IEEE Transactions on Power Electronics*, vol. 36, no. 9, pp. 10 660–10 672, Sep. 2021. DOI: 10.1109/TPEL.2021.3060106.